3-D elastic modeling with surface topography by a Chebychev spectral method

E. Tessmer* and D. Kosloff‡

ABSTRACT

The 3-D numerical Chebychev modeling scheme accounts for surface topography. The method is based on spectral derivative operators. Spatial differencing in horizontal directions is performed by the Fourier method, whereas vertical derivatives are carried out by a Chebychev method that allows for the incorporation of boundary conditions into the numerical scheme. The method is based on the velocity-stress formulation. The implementation of surface topography is done by mapping a rectangular grid onto a curved grid. Boundary conditions are applied by means of characteristic variables. The study of surface effects of seismic wave propagation in the presence of surface topography is important, since nonray effects such as diffractions and scattering at rough surfaces must be considered. Several examples show this. The 3-D modeling alogrithm can serve as a tool for understanding these phenomena since it computes the full wavefield.

INTRODUCTION

Surface topography and the weathered zone have great influence on seismic reflection surveys. In cases of mild topography and low-velocity heterogeneities the effects of topography and the weathering zone can be removed by static corrections. However, in cases of a rough surface and a heterogeneous weathering layer, the seismograms are contaminated by diffractions, and the behavior of the ground roll becomes more difficult.

If the wavelengths of the topography and the seismic energy are of the same order, nonray wave propagation phenomena occur and body waves as well as surface waves are scattered at the highs and lows of the surface topography. In such cases, static corrections cannot remove these topographic effects.

As a result of scattering, surface wave amplitudes decay more rapidly in the presence of surface topography. These effects are present both in global seismology and in reflection seismology.

Various direct methods can be applied to the surface topography problem in connection with high material heterogeneity, e.g., finite differences and finite elements. However, these methods are usually of low order.

Higher order finite-difference methods that are based on staggered grids cannot use this approach for the incorporation of surface topography, since not all the variables (i.e., particle velocities and stresses) are available at the same grid node. Therefore some interpolation would be necessary, which in turn degrades the accuracy of finite-difference operators.

Generally, it is difficult to incorporate boundary conditions into spectral methods accurately. An exception is the Chebychev spectral method (Kosloff et al., 1990) which is of high accuracy. This method can handle the free surface boundary condition correctly by using the concept of characteristic variables.

The method presented here is based on the Chebychev spectral method. It is an extension of the 2-D algorithm given in a previous paper (Tessmer et al., 1992). The numerical examples demonstrate the relevance of 3-D modeling with surface topography.

EQUATIONS OF MOTION

The 3-D equations of motion can be written as:

$$\rho \frac{\partial^2 u_i}{\partial t^2} = \frac{\partial \sigma_{ij}}{\partial x_j} + f_i, \tag{1}$$

where in the general elastic case the stresses σ_{ij} are given by

$$\sigma_{ij} = c_{ijk\ell} \varepsilon_{k\ell}, \tag{2}$$

and f_i denotes the body forces. The strains $\varepsilon_{k\ell}$ are defined as

$$\varepsilon_{ij} = \frac{1}{2}\left(\frac{\partial u_i}{\partial x_j} + \frac{\partial u_j}{\partial x_i}\right). \qquad (3)$$

In the case of isotropic elastic behavior, the stress strain relation reduces to

$$\sigma_{ij} = \lambda \varepsilon_{kk}\delta_{ij} + 2\mu\varepsilon_{ij}, \qquad (4)$$

where λ and μ are the Lamé parameters and ρ denotes the density. Parameters λ and μ are related to the seismic velocities v_P and v_S by $v_P = \sqrt{(\lambda + 2\mu)/\rho}$ and $v_s = \sqrt{\mu/\rho}$.

Equation (1) is a system of three coupled PDEs of second order in time where the displacements u_x, u_y, and u_z are the unknowns. The system of second-order partial-differential equations (PDEs) can be rewritten into a system of first-order PDEs in time. We then obtain a system of nine equations with the particle velocities $\dot{u}_i$ and the stresses σ_{ij} as the unknowns (Bayliss et al., 1986; Virieux, 1986):

$$\rho\frac{\partial \dot{u}_x}{\partial t} = \frac{\partial \sigma_{xx}}{\partial x} + \frac{\partial \sigma_{xy}}{\partial y} + \frac{\partial \sigma_{xz}}{\partial z} + f_x,$$

$$\rho\frac{\partial \dot{u}_y}{\partial t} = \frac{\partial \sigma_{xy}}{\partial x} + \frac{\partial \sigma_{yy}}{\partial y} + \frac{\partial \sigma_{yz}}{\partial z} + f_y,$$

$$\rho\frac{\partial \dot{u}_z}{\partial t} = \frac{\partial \sigma_{xz}}{\partial x} + \frac{\partial \sigma_{yz}}{\partial y} + \frac{\partial \sigma_{zz}}{\partial z} + f_z,$$

$$\frac{\partial \sigma_{xx}}{\partial t} = \lambda\left(\frac{\partial \dot{u}_x}{\partial x} + \frac{\partial \dot{u}_y}{\partial y} + \frac{\partial \dot{u}_z}{\partial z}\right) + 2\mu\frac{\partial \dot{u}_x}{\partial x},$$

$$\frac{\partial \sigma_{yy}}{\partial t} = \lambda\left(\frac{\partial \dot{u}_x}{\partial x} + \frac{\partial \dot{u}_y}{\partial y} + \frac{\partial \dot{u}_z}{\partial z}\right) + 2\mu\frac{\partial \dot{u}_y}{\partial y}, \qquad (5)$$

$$\frac{\partial \sigma_{zz}}{\partial t} = \lambda\left(\frac{\partial \dot{u}_x}{\partial x} + \frac{\partial \dot{u}_y}{\partial y} + \frac{\partial \dot{u}_z}{\partial z}\right) + 2\mu\frac{\partial \dot{u}_z}{\partial z},$$

$$\frac{\partial \sigma_{xy}}{\partial t} = \mu\left(\frac{\partial \dot{u}_x}{\partial y} + \frac{\partial \dot{u}_y}{\partial x}\right),$$

$$\frac{\partial \sigma_{xz}}{\partial t} = \mu\left(\frac{\partial \dot{u}_x}{\partial z} + \frac{\partial \dot{u}_z}{\partial x}\right),$$

$$\frac{\partial \sigma_{yz}}{\partial t} = \mu\left(\frac{\partial \dot{u}_y}{\partial z} + \frac{\partial \dot{u}_z}{\partial y}\right).$$

SURFACE TOPOGRAPHY

The surface topography is introduced by mapping a 3-D rectangular grid onto a curved grid. The auxiliary rectangular grid has the spatial coordinates ξ, v, and ζ, whereas the physical curved grid has the coordinates x, y, and z. A similar approach was used by Fornberg (1988) to represent curved interfaces in case of 2-D modeling.

We begin with the mapping functions:

$$x(\xi, v, \zeta) = \xi,$$

$$y(\xi, v, \zeta) = v,$$

and

$$z(\xi, v, \zeta) = z_0(\xi, v) + \frac{\zeta}{\zeta_{max}}(z_{max} - z_0(\xi, v)), \qquad (6)$$

where $z_0(\xi, v)$ is a topographic function that describes the elevation above some reference level. Parameter z_{max} is the maximum depth of the model assumed to have a plane horizontal bottom.

The mapping chosen in this paper results in a vertical linear stretch of the computational grid. However, nonlinear stretching functions can also be applied. For simplicity, Figure 1 illustrates the mapping for the 2-D case.

VELOCITY-STRESS FORMULATION ON THE CURVED GRID

We rewrite the equations of motion (1) as a system of first-order equations in time (Bayliss et al., 1986; Virieux, 1986) and apply the chain rule to account for the stretching of the grid in the z-direction according to equation (6):

$$\rho\frac{\partial \dot{u}_x}{\partial t} = \frac{\partial \sigma_{xx}}{\partial \xi} + \frac{\partial \sigma_{xx}}{\partial \zeta}\frac{\partial \zeta}{\partial x} + \frac{\partial \sigma_{xy}}{\partial v} + \frac{\partial \sigma_{xy}}{\partial \zeta}\frac{\partial \zeta}{\partial y} + \frac{\partial \sigma_{xz}}{\partial \zeta}\frac{\partial \zeta}{\partial z} + f_x,$$

$$\rho\frac{\partial \dot{u}_y}{\partial t} = \frac{\partial \sigma_{xy}}{\partial \xi} + \frac{\partial \sigma_{xy}}{\partial \zeta}\frac{\partial \zeta}{\partial x} + \frac{\partial \sigma_{yy}}{\partial v} + \frac{\partial \sigma_{yy}}{\partial \zeta}\frac{\partial \zeta}{\partial y} + \frac{\partial \sigma_{yz}}{\partial \zeta}\frac{\partial \zeta}{\partial z} + f_y,$$

$$\rho\frac{\partial \dot{u}_z}{\partial t} = \frac{\partial \sigma_{xz}}{\partial \xi} + \frac{\partial \sigma_{xz}}{\partial \zeta}\frac{\partial \zeta}{\partial x} + \frac{\partial \sigma_{yz}}{\partial v} + \frac{\partial \sigma_{yz}}{\partial \zeta}\frac{\partial \zeta}{\partial y} + \frac{\partial \sigma_{zz}}{\partial \zeta}\frac{\partial \zeta}{\partial z} + f_z,$$
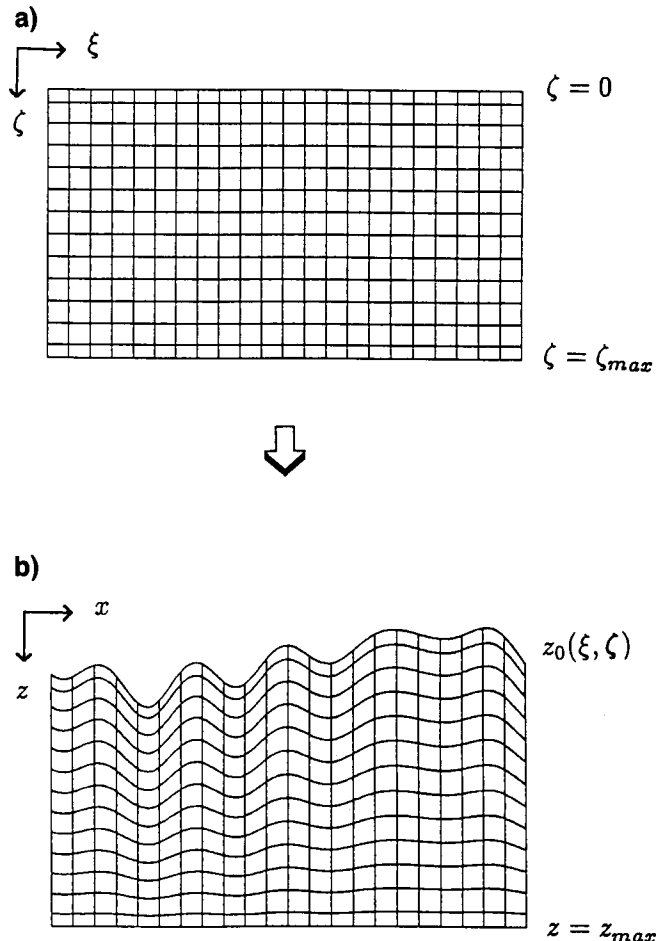

FIG. 1. Mapping of a rectangular grid ($\xi\zeta$-space) (a) onto a curved grid (xz-space) (b) with linear vertical stretching.

$$\frac{\partial \sigma_{xx}}{\partial t} = \lambda \left(\frac{\partial \dot{u}_x}{\partial \xi} + \frac{\partial \dot{u}_x}{\partial \zeta} \frac{\partial \zeta}{\partial x} + \frac{\partial \dot{u}_y}{\partial v} + \frac{\partial \dot{u}_y}{\partial \zeta} \frac{\partial \zeta}{\partial y} + \frac{\partial \dot{u}_z}{\partial \zeta} \frac{\partial \zeta}{\partial z} \right)$$
$$+ 2\mu \left(\frac{\partial \dot{u}_x}{\partial \xi} + \frac{\partial \dot{u}_x}{\partial \zeta} \frac{\partial \zeta}{\partial x} \right),$$

$$\frac{\partial \sigma_{yy}}{\partial t} = \lambda \left(\frac{\partial \dot{u}_x}{\partial \xi} + \frac{\partial \dot{u}_x}{\partial \zeta} \frac{\partial \zeta}{\partial x} + \frac{\partial \dot{u}_y}{\partial v} + \frac{\partial \dot{u}_y}{\partial \zeta} \frac{\partial \zeta}{\partial y} + \frac{\partial \dot{u}_z}{\partial \zeta} \frac{\partial \zeta}{\partial z} \right)$$
$$+ 2\mu \left(\frac{\partial \dot{u}_y}{\partial v} + \frac{\partial \dot{u}_y}{\partial \zeta} \frac{\partial \zeta}{\partial y} \right),$$

$$\frac{\partial \sigma_{zz}}{\partial t} = \lambda \left(\frac{\partial \dot{u}_x}{\partial \xi} + \frac{\partial \dot{u}_x}{\partial \zeta} \frac{\partial \zeta}{\partial x} + \frac{\partial \dot{u}_y}{\partial v} + \frac{\partial \dot{u}_y}{\partial \zeta} \frac{\partial \zeta}{\partial y} + \frac{\partial \dot{u}_z}{\partial \zeta} \frac{\partial \zeta}{\partial z} \right)$$
$$+ 2\mu \left(\frac{\partial \dot{u}_z}{\partial \zeta} \frac{\partial \zeta}{\partial z} \right),$$

$$\frac{\partial \sigma_{xy}}{\partial t} = \mu \left(\frac{\partial \dot{u}_x}{\partial v} + \frac{\partial \dot{u}_x}{\partial \zeta} \frac{\partial \zeta}{\partial y} + \frac{\partial \dot{u}_y}{\partial \xi} + \frac{\partial \dot{u}_y}{\partial \zeta} \frac{\partial \zeta}{\partial x} \right),$$

$$\frac{\partial \sigma_{xz}}{\partial t} = \mu \left(\frac{\partial \dot{u}_x}{\partial \zeta} \frac{\partial \zeta}{\partial z} + \frac{\partial \dot{u}_z}{\partial \xi} + \frac{\partial \dot{u}_z}{\partial \zeta} \frac{\partial \zeta}{\partial x} \right),$$

$$\frac{\partial \sigma_{yz}}{\partial t} = \mu \left(\frac{\partial \dot{u}_y}{\partial \zeta} \frac{\partial \zeta}{\partial z} + \frac{\partial \dot{u}_z}{\partial v} + \frac{\partial \dot{u}_z}{\partial \zeta} \frac{\partial \zeta}{\partial y} \right). \tag{7}$$

For the computation of equation (7), we need the terms $\partial\zeta/\partial x$, $\partial\zeta/\partial y$, and $\partial\zeta/\partial z$ given by:

$$\frac{\partial \zeta}{\partial x} = -\frac{\partial z}{\partial \xi} \cdot \left(\frac{\partial z}{\partial \zeta} \right)^{-1},$$

$$\frac{\partial \zeta}{\partial y} = -\frac{\partial z}{\partial v} \cdot \left(\frac{\partial z}{\partial \zeta} \right)^{-1}, \tag{8}$$

$$\frac{\partial \zeta}{\partial z} = \left(\frac{\partial z}{\partial \zeta} \right)^{-1}.$$

SPATIAL DISCRETIZATION

The variables u_i, σ_{ij}, and the material parameters λ, μ, and ρ are discretized on a spatial grid, where the grid spacings in the x- and y-directions are uniform and nonuniform in the vertical direction.

The solution scheme is the same as in Tessmer et al. (1992) for the 2-D case. Differentiation with respect to the horizontal directions is carried out by the Fourier method (Gazdag, 1981; Kosloff and Baysal, 1982), while the vertical derivatives are performed by a Chebychev derivative operator (Kosloff et al., 1990). For the time integration, a fourth-order Taylor expansion of the formal solution with time stepping is used. Complete details of the numerical algorithm can be found in Tessmer et al. (1992).

FREE-SURFACE BOUNDARY CONDITIONS WITH TOPOGRAPHY

The boundary conditions at the free surface are zero normal tractions. In a local coordinate system with the z'-axis normal to the surface element, this reads:

$$\sigma'_{xz} = \sigma'_{yz} = \sigma'_{zz} = 0. \tag{9}$$

Requiring the above boundary conditions implies modifications of the remaining variables by characteristic treatment (Gottlieb et al., 1982). The modified variables then read (Tessmer et al., 1990):

$$\sigma'_{yy}{}^{(new)} = \sigma'_{yy}{}^{(old)} - \frac{\lambda}{\lambda + 2\mu} \sigma'_{zz}{}^{(old)},$$

$$\sigma'_{xx}{}^{(new)} = \sigma'_{xx}{}^{(old)} - \frac{\lambda}{\lambda + 2\mu} \sigma'_{zz}{}^{(old)},$$

$$\dot{u}'_y{}^{(new)} = \dot{u}'_y{}^{(old)} + \frac{\sigma'_{yz}{}^{(old)}}{\sqrt{\rho\mu}}, \tag{10}$$

$$\dot{u}'_x{}^{(new)} = \dot{u}'_x{}^{(old)} + \frac{\sigma'_{xz}{}^{(old)}}{\sqrt{\rho\mu}},$$

$$\dot{u}'_z{}^{(new)} = \dot{u}'_z{}^{(old)} + \frac{\sigma'_{zz}{}^{(old)}}{\sqrt{\rho(\lambda + 2\mu)}}.$$

The superscripts $^{(old)}$ and $^{(new)}$ denote the values of the variables at the free surface before and after the correction, respectively. These corrections have to be applied to stresses and particle velocities. Only σ'_{xy} remains unchanged.

Before the application of the characteristic treatment, the particle velocities $\dot{u}_i$ and the stresses σ_{ij}, which are given in the (x, y, z)-coordinate system, must be transformed into the local (x', y', z')-coordinate system where the z'-axis is normal to the surface element. The transformation into the local (x, y, z)-coordinate system is given by

$$\dot{u}'_i = a_{ij} \dot{u}_j,$$

and

$$\sigma'_{ij} = a_{ik} a_{j\ell} \sigma_{k\ell}, \tag{11}$$

with $i, j, k, \ell = 1, 2, 3$, where a_{ij} are the components of a 3×3 rotation matrix, and the indices 1, 2, and 3 correspond
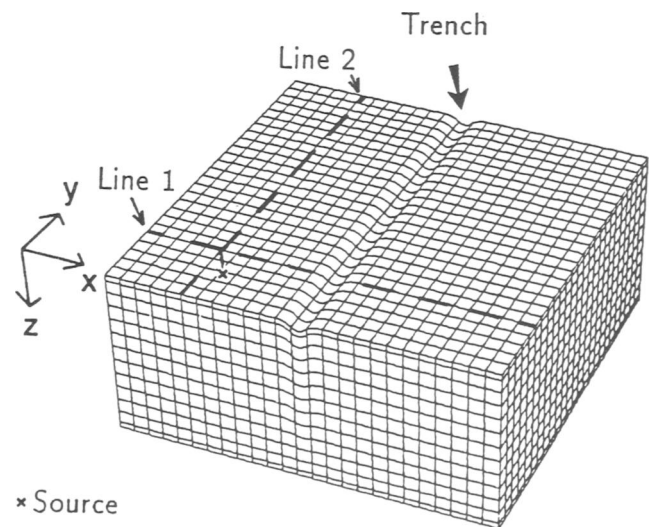

FIG. 2. The trench model: A homogeneous half-space with a surface trench. The size of the model is 1250 m × 1250 m × 570 m (125 × 125 × 65 gridnotes). The depth of the trench is 28.5 m. The source location is 52 m below the surface. Two receiver lines are marked.

to the x-, y-, and z-coordinates, respectively. Here, $\dot{u}'_i$ and σ'_{ij} are, respectively, the particle velocities and the stress components in the rotated local (x', y', z')-coordinate system. The elements of the rotation matrix are given by:

$$a_{11} = \cos\vartheta + \alpha^2(1 - \cos\vartheta),$$

$$a_{12} = \alpha\beta(1 - \cos\vartheta),$$

$$a_{13} = -\beta\sin\vartheta,$$

$$a_{21} = \alpha\beta(1 - \cos\vartheta),$$

$$a_{22} = \cos\vartheta + \beta^2(1 - \cos\vartheta),$$

$$a_{23} = \alpha\sin\vartheta,$$

$$a_{31} = \beta\sin\vartheta,$$

$$a_{32} = -\alpha\sin\vartheta,$$

$$a_{33} = \cos\vartheta,$$

where

$$\cos\vartheta = \frac{\mathbf{n}\cdot\mathbf{e}_z}{|\mathbf{n}|}$$

$$\alpha = \frac{\mathbf{g}\cdot\mathbf{e}_x}{|\mathbf{g}|}, \quad \beta = \frac{\mathbf{g}\cdot\mathbf{e}_y}{|\mathbf{g}|}, \quad \text{and} \quad \mathbf{g} = \mathbf{n}\times\mathbf{e}_z.$$

The normal vector on the surface element is given by:

$$\mathbf{n} = \left(\frac{\partial z_0}{\partial x}, \frac{\partial z_0}{\partial y}, -1\right)^T.$$

Vectors $\mathbf{e}_x$, $\mathbf{e}_y$, and $\mathbf{e}_z$ are unit vectors in the x-, y-, and z-directions, respectively.

After the modifications according to equation (10), the variables must be transformed back into the original (x, y, z)-coordinate system.

EXAMPLES

To demonstrate the effects of surface topography, three cases of irregular surfaces are investigated. The first example has a trench at its surface along the y-direction (Figure 2). The width and depth of the trench is of the size of the dominant wavelength. This is a situation where the wave phenomena that occur cannot be treated by ray-tracing methods. In a second example, a local depression at the surface is modeled (Figure 7). Also in this case the wavelength and the irregularity are of comparable size. The last example deals with sinusoidal surface topography in both the x- and y-direction (Figure 9). Here the wavelength of the topography is larger than the dominant wavelength of the seismic signal. The respective seismic velocities for the P- and S-waves are 2000 m/s and 1155 m/s in all examples. A vertical point force is applied ten grid points (52 m) below the surface. The source function has a cutoff frequency of 35 Hz with a Ricker-like time history. For simplicity all examples are made up of homogeneous half-spaces.

Trench

The trench model is shown in Figure 2. The numerical model contains $125 \times 125 \times 65$ grid nodes in the x-, y-, and z-direction, respectively. The grid spacings are 10 m in the x- and y-directions and in the z-direction are in the center of the grid. The total volume is 1250 m $\times$ 1250 m $\times$ 570 m. (The vertical spacing varies with depth because of the Chebychev derivative operator and is smaller toward the free surface and the bottom of the model.)

The total propagation time is 800 ms with timesteps of 1 ms. The model has a trench at the surface along the y-direction (Figure 2). The depth of the trench is 28.5 m, i.e., approximately $\frac{1}{4}$ of the dominant wavelength.
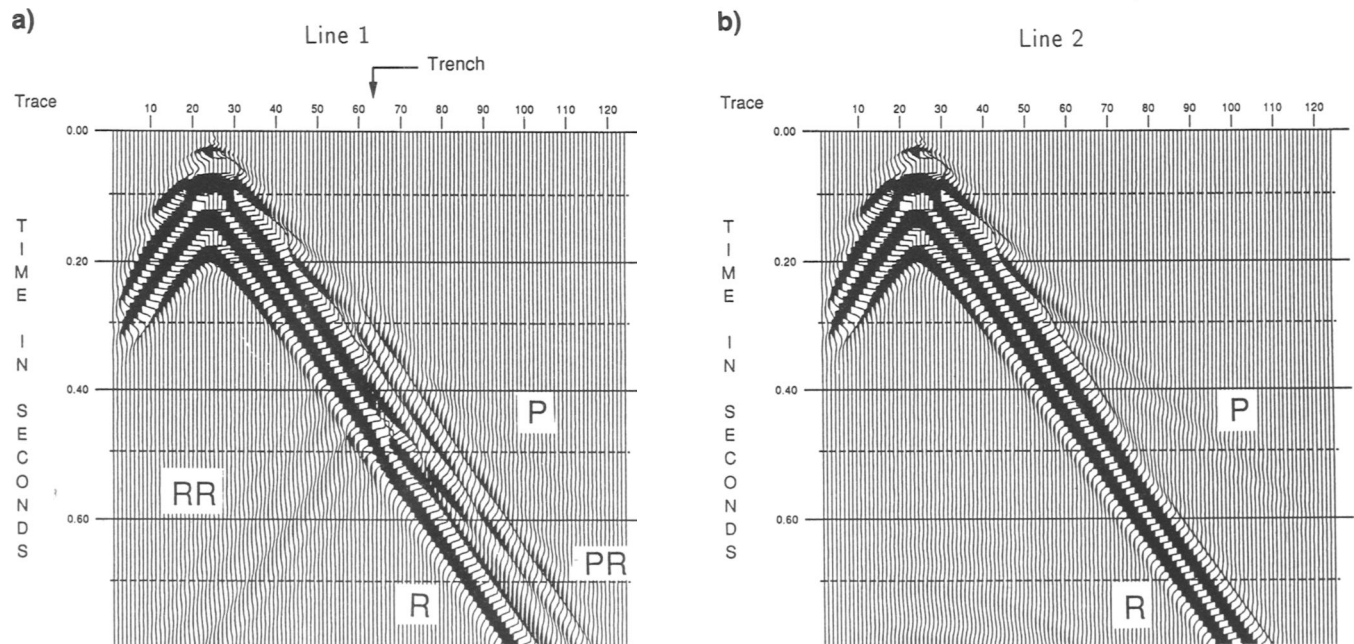

FIG. 3. Seismogram sections at the surface of the trench model of the vertical component in the x-direction (a) and in the y-direction (b).
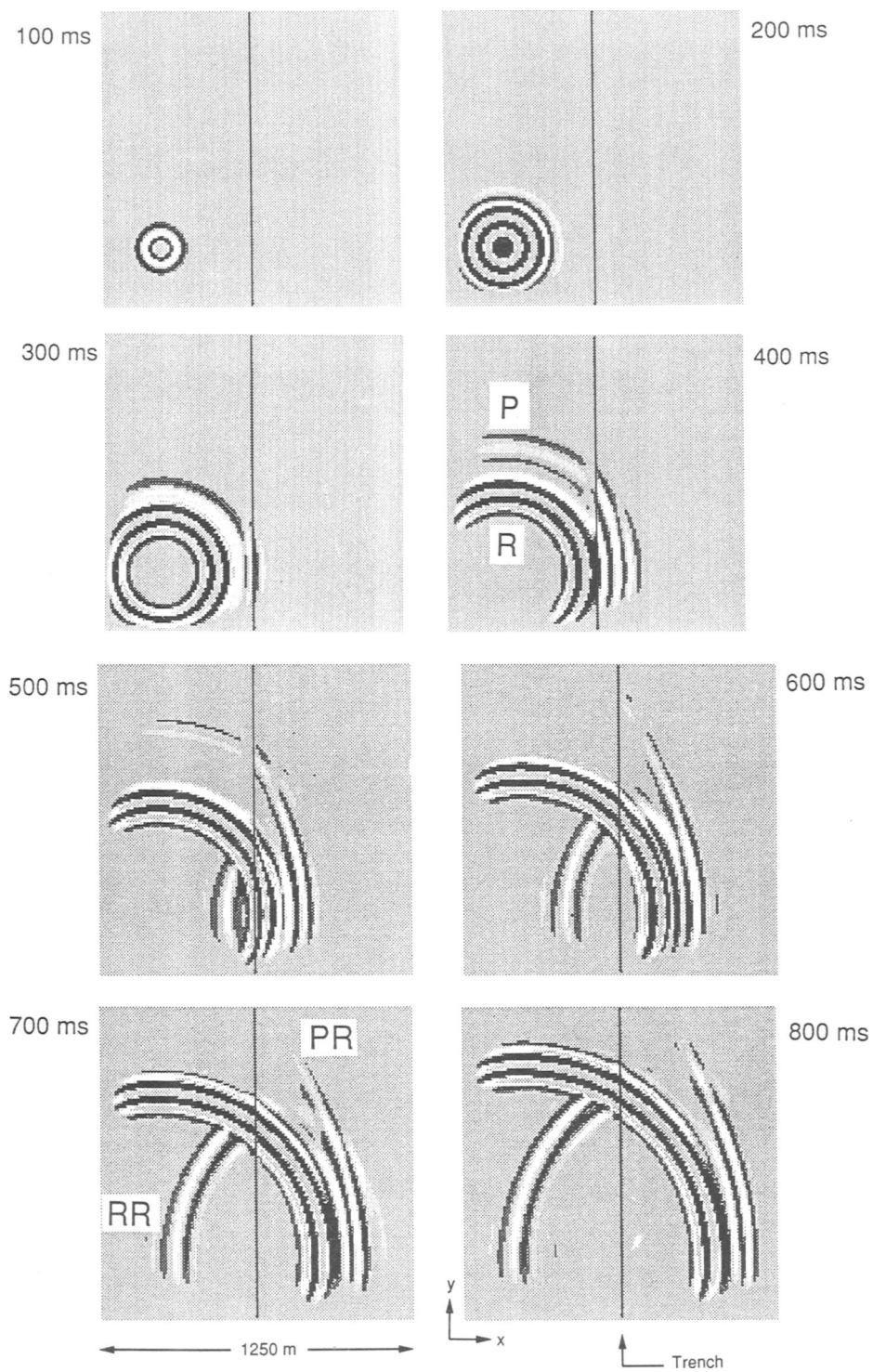
FIG. 4. Snapshots of the vertical component of the wavefield at the surface (xy-plane) of the trench model. (The solid line marks the trench axis.)

At two receiver lines, parallel and perpendicular to the trench, seismograms were recorded (Figure 3). The seismogram section (vertical component) in the x-direction (Line 1) shows the direct P-wave and a high-amplitude Rayleigh wave (R). As a result of scattering at the trench, the amplitude of the Rayleigh wave is reduced in the right-hand part of the sections. In addition, in front of the ordinary Rayleigh wave a secondary Rayleigh wave (PR) induced by the scattering of the direct P-wave can be observed. Some energy is scattered back to the left-hand side (RR). The section in the y-direction (Line 2) shows undisturbed P- and Rayleigh waves.

Snapshots of the wavefield of horizontal (xy-) plane at different propagation times are displayed in Figure 4. The xy-snapshots represent the wavefield at the surface. In the beginning the wavefield propagates undisturbed along the free surface. At 400 ms the direct P-wave hits the trench and generates a secondary Rayleigh wave (PR), which travels in front of the ordinary Rayleigh wave. This can be seen clearly in the later snapshots (500 − 800 ms). In addition, a reflected Rayleigh wave (RR) can be observed. The direct P-waves and Rayleigh waves (R, RR, and PR) are marked in the figure.

Figure 5 shows the vertical component of the wavefield in the vertical (xz-) plane. The xz-plane contains receiver line 1 and the source location. At about 300 ms propagation time, the P-wave arrives at the trench and is scattered. At about 400 ms, the S-wave hits the trench and is diffracted. The snapshots between 600 and 800 ms show these diffracted P- and S-waves.

Figure 6 shows the vertical component of the wavefield in the vertical (yz-) plane. The xy-plane contains receiver line 2 and the source location. The wavefield propagates undisturbed for a long time since in this direction no surface inhomogeneities appear. Direct P-, S-, and Rayleigh waves can be observed. Additionally, at 500 and 600 ms a headwave (H) can be found in the photos. This headwave is a shear wave and is guided along the surface by the P-wave. At later times (700 and 800 ms), side reflections appear in the photo plane. These are caused by the reflected Rayleigh wave. This is a real 3-D effect that could not be found in 2-D modeling results.

Depression

Figure 7 shows the depression model. The depth of the depression is 22 m. The numerical model contains $125 \times 125 \times 51$ grid nodes in the x-, y-, and z-directions, respectively. The grid spacings are 10 m. The photos in Figure 8 show the vertical component of the wavefield in the horizontal (xy-) plane. In the beginning, the waves propagate undisturbed. At 400 ms propagation time and later, a circular diffracted wave originating at the depression can be observed. The strong amplitudes appearing at the source region at later times are caused by reflections from the model bottom, which in this case has rigid boundary conditions.

Sinusoidal topography

Figure 9 shows the sinusoidal topography model. The numerical model contains $125 \times 125 \times 51$ grid nodes in the x-, y-, and z-direction, respectively. The grid spacings are
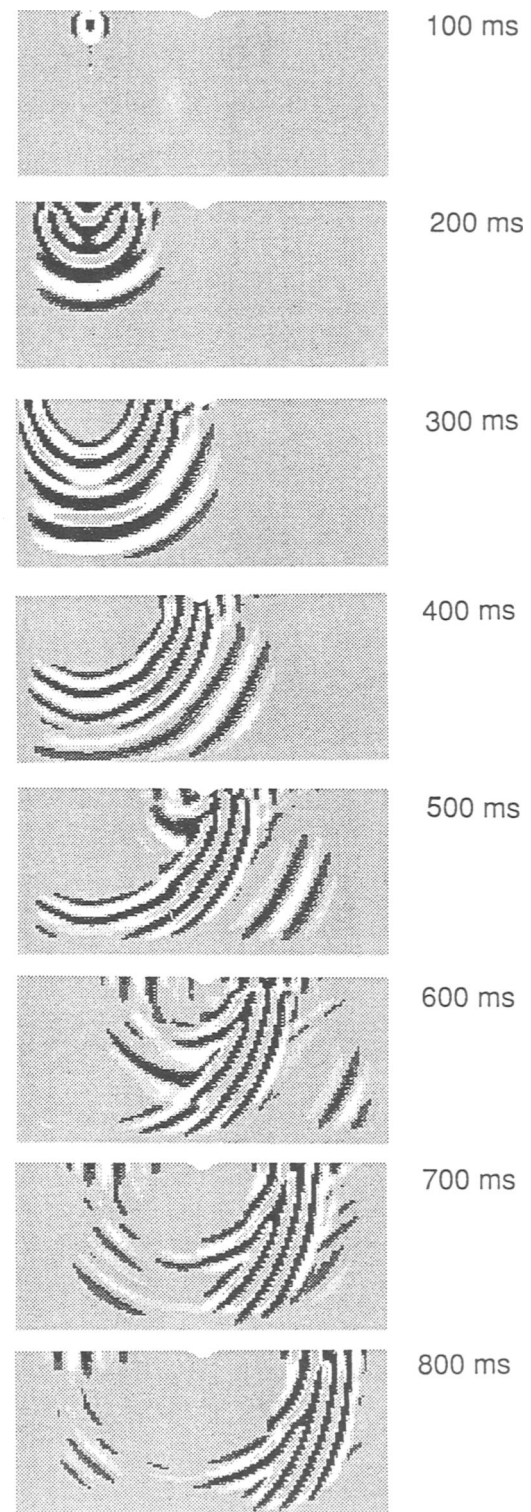

FIG. 5. Snapshots of the vertical component of the wavefield in the vertical (xz-) plane of the trench model, which contains receiver line 1 and the source.
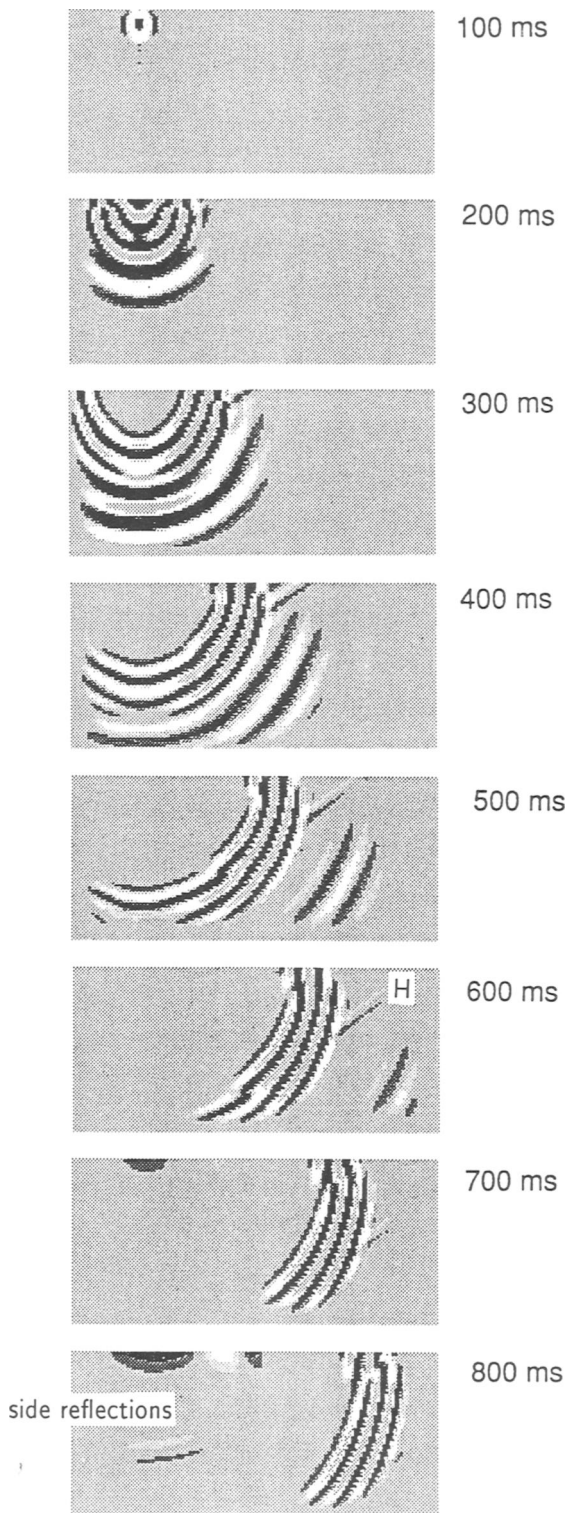
FIG. 6. Snapshots of the vertical component of the wave-field in the vertical (yz-) plane of the trench model, which contains receiver line 2 and the source.

10 m in all directions. The amplitude of the topography is ±22 m. Its wavelength is 250 m. Photos of the vertical component of the wavefield are shown in Figure 10. In the beginning, almost circular wavefronts are preserved. However, with progressive time caused by backscattering at the highs and lows of the topography, the wavefield appears rather complicated, and it is difficult to attribute events to certain wave types.

Seismogram sections for the three components of particle velocity are shown in Figure 11. The strongest event in all the sections is the Rayleigh wave. Also in this example, rigid boundary conditions at the model bottom are implemented, which leads to strong reflections. It is remarkable that the y-component (crossline) shows energy at all. (The amplitudes of the three sections are of the same order of magnitude.) This is a consequence of reflections from the irregular free surface. In case of a flat free surface, the y-component would not show any energy, because of the radiation pattern of the source.

CONCLUSION

A spectral method that can handle 3-D surface topography with high accuracy has been presented. The surface topography is introduced via mapping rectangular grids to curved grids. The accurate application of the free surface boundary conditions is done using characteristic variables after rotation of the solution vector into a local coordinate system, which has its z-axis normal on the surface. After application of the boundary conditions, the solution vector is rotated back into the original coordinate system.

The method presented permits the investigation of near-surface effects stemming from wave propagation phenomena caused by a rough surface. The latter include diffractions, scattering, multiple reflections, and converted waves.

The method can be used to generate synthetic data, which can be used to study the influence of surface topography on seismic processing steps such as static corrections and migration techniques.
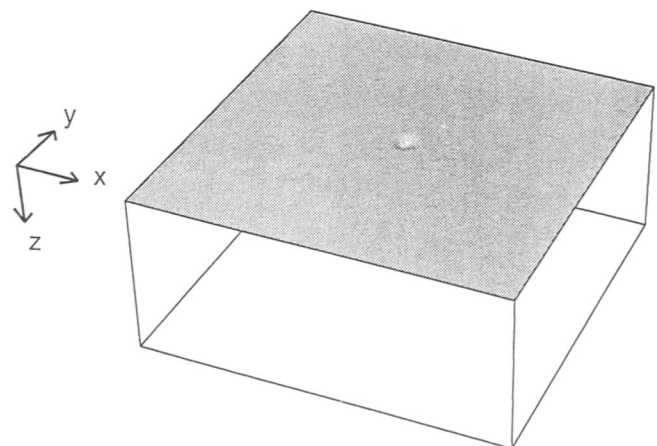

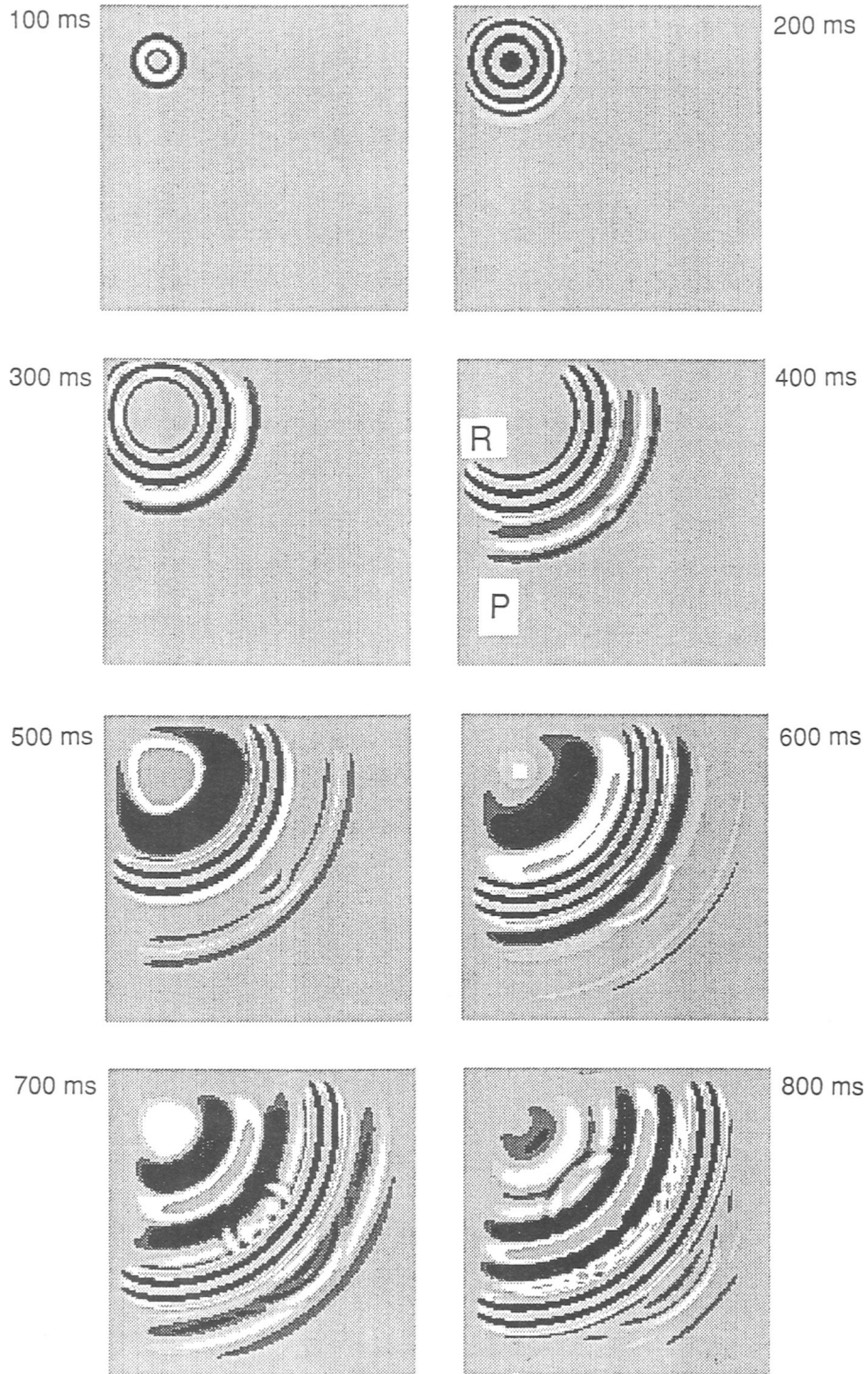FIG. 7. The depression model: Homogeneous half-space with a surface depression of 22 m depth.

FIG. 8. Snapshots of the vertical component of the wavefield at the surface (xy-plane) of the depression model.

REFERENCES

Bayliss, A., Jordan, K. E., LeMesurier, B. J., and Turkel, E., 1986, A fourth-order accurate finite-difference scheme for the computation of elastic waves: Bull. Seis. Soc. Am., **76**, 1115–1132.

Fornberg, B., 1988, The pseudospectral method: Accurate representation of interfaces in elastic wave calculations: Geophysics, **53**, 625–637.

Gazdag, J., 1981, Modeling of the acoustic wave equation with transform methods: Geophysics, **46**, 854–859.

Gottlieb, D., Gunzburger, M., and Turkel, E., 1982, On numerical boundary treatment of hyperbolic systems for finite-difference and finite-element methods: SIAM J. Num. Anal., **19**, 671–682.

Kosloff, D., and Baysal, E., 1982, Forward modeling by a Fourier method: Geophysics, **47**, 1402–1412.

Kosloff, D., Kessler, D., Filho, A. Q., Tessmer, E., Behle, A., and Strahilevitz, R., 1990, Solution of the equations of dynamic elasticity by a Chebychev spectral method: Geophysics, **55**, 734–748.

Tessmer, E., Kosloff, D., and Behle, A., 1992, Elastic wave propagation simulation in the presence of surface topography: Geophys. J. Int., **108**, 621–632.

Tessmer, E., Tessmer, G., Kosloff, D., and Behle, A., 1990. 3-D elastic modeling by a Chebychev spectral method: 60th Ann. Internat. Mtg., Soc. Expl. Geophys., Expanded Abstracts, 1049–1052.

Virieux, J., 1986, P-SV wave propagation in heterogeneous media: Velocity-stress finite-difference method: Geophysics, **51**, 888–901.

FIG. 9. The sinusoidal surface topography model: Homogeneous half-space with sinusoidal surface topography with an amplitude of ±22 m.
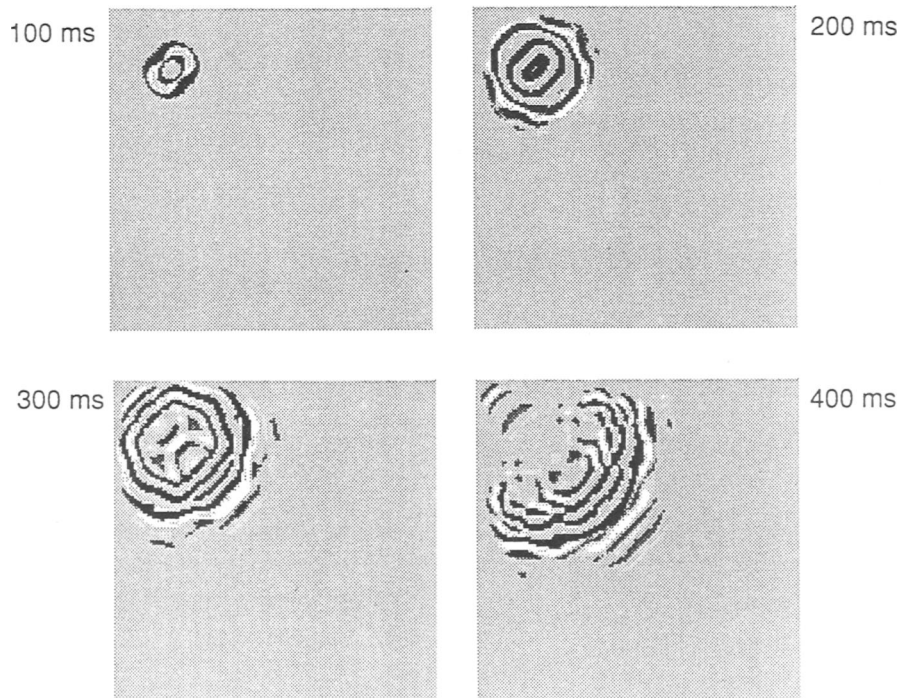

FIG. 10. Snapshots of the vertical component of the wavefield at the surface (xy-plane) of the sinusoidal surface topography model.
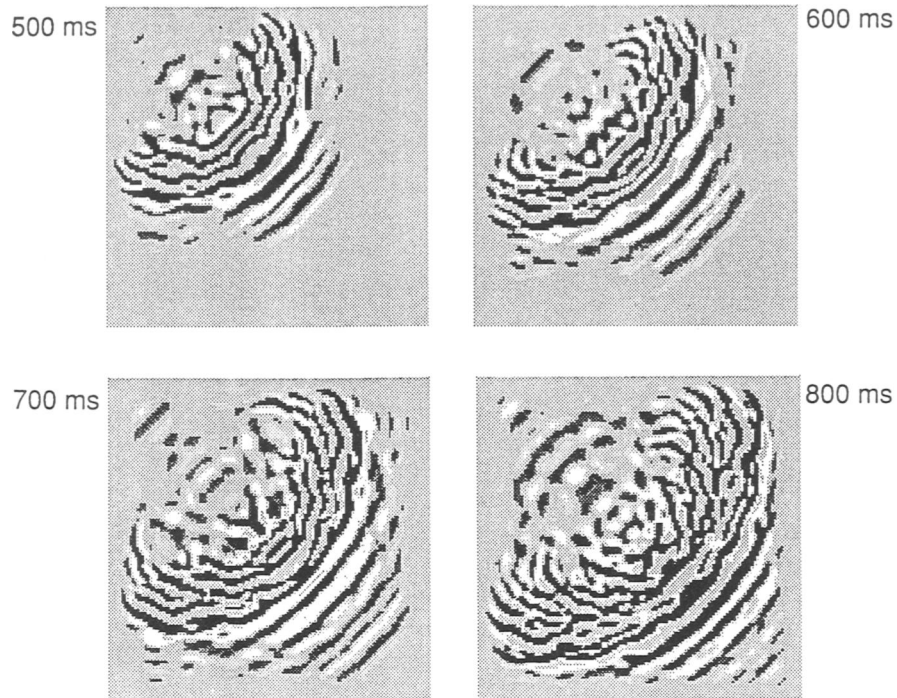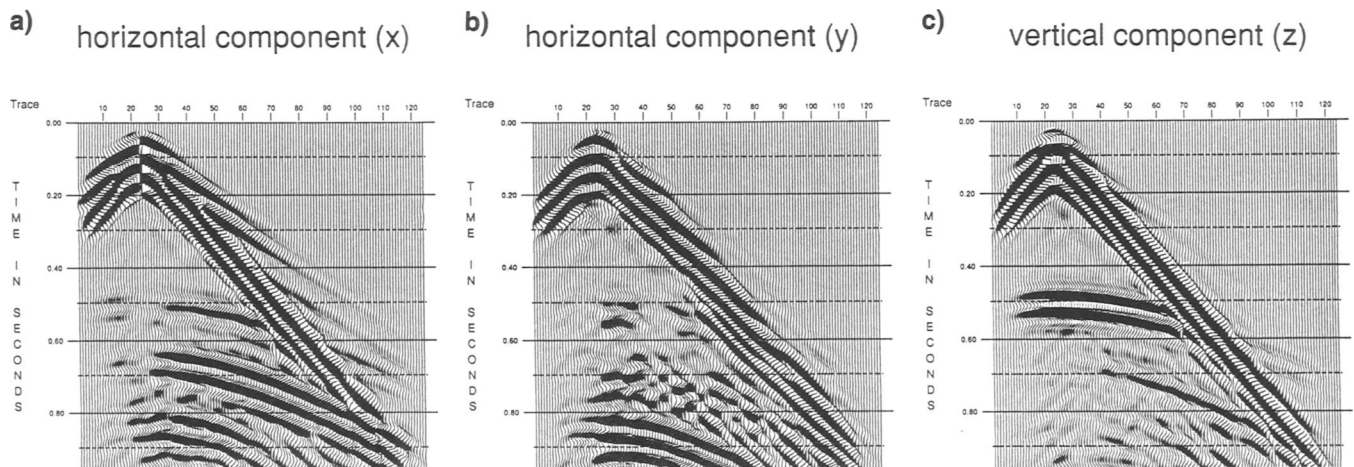
FIG. 10. (continued)

FIG. 11. Seismogram sections of the three components of the particle velocity at the surface. (a) In-line component (x), (b) crossline component (y), and (c) vertical component (z).